Microwave Omnidirectional Angle-of-Arrival Measurement based on an Optical Ten-Port Receiver

Yuanqi Yang, Zhenzhou Tang, *Member, IEEE*, Zhongyang Xu, *Member, IEEE*, Cui Yu, and Shilong Pan, *Senior Member, IEEE*

***Abstract*—A photonics-based scheme to measure microwave omnidirectional angle-of-arrival (AOA) is proposed. In the proposed system, an optical carrier is split into two branches. In one branch, the optical carrier is frequency-shifted by an acousto-optic modulator (AOM) and led to a Mach-Zehnder modulator (MZM) which is modulated by an echo signal from an antenna. In the other branch, a polarization-division-multiplexed MZM (PDM-MZM) is used to imprint two different echo signals received by another two antennas placed above and to the right of the previous antenna, respectively. Then, an optical bandpass filter is connected after each modulator to select one of the 1st-order sidebands. The selected sidebands are sent to an optical ten-port receiver, which is consisted of a dual-polarization 90-degree optical hybrid and four balanced photodetectors (BPDs). After processing the low-frequency signals from the orthogonal outputs of the ten-port optical receiver, the azimuth and altitude AOA of the received RF signal could be simultaneously obtained. In a proof-of-concept experiment, the measurement error of the altitude AOA is less than $\pm 1.63^\circ$ within the angular range of $-48.08^\circ \sim 56.43^\circ$, and the measurement error of the azimuth AOA is smaller than $\pm 3.09^\circ$ when the angular range is from -68.35° to 64.65°.**

***Index Terms*—Angle of arrival (AOA), coherent I/Q detection, microwave photonics, multi-port receiver, optical hybrid.**

I. Introduction

There is a general consensus that the capabilities of the six-generation (6G) communication system will not limit to communication, but also includes computing [1], control, localization, and sensing [2]. With the development of 6G, an unprecedented proliferation of new Internet of Everything (IoE) [3] services will gradually mature, including the extended reality (XR) services, cardiac activity sensing [4], autonomous driving [5], gesture sensing [6], [7], brain-computer interfaces [8], and connected autonomous systems. To fulfill the aforementioned requirements, wireless sensing systems will play a more and more important role owing to their flexibility and non-contact characteristics. Specially, the angle of arrival (AOA) is one of the most important parameters to identify the direction of the target in the wireless sensing systems. In [9], an AOA estimation based on a dual channel 6-port receiver with a bandwidth coving from 2 to 18 GHz is proposed. The entire AOA measurement error is as low as $\pm 0.518^\circ$. Moreover, 2-D AOA estimation is realized in [10], where the azimuth and altitude AOAs are measured from -5° to 5°. The standard deviation of the measured altitude AOA is around 0.2°, while that of the azimuth AOA is about 0.4°. However, conventional electrical AOA estimation methods have limited bandwidths, and suffer greatly from the electromagnetic interference, especially when the wireless sensing system is moving to a higher frequency band to explore more spectral resources. Thanks to the intrinsic advantages in terms of wide instantaneous bandwidth, low transmission loss and immunity to electromagnetic interference, microwave photonic AOA estimation has been regarded as a promising solution [11]–[16].

In general, photonic-based microwave AOA measurement can be classified into two categories: In the first category, the echo signals are firstly downconverted to intermediate frequency (IF) signals, and digital signal processing is then employed to extract the phase difference between the IF signals. Since the phase difference is related to the AOA of the incoming microwave signal, the AOA information can be finally calculated from the obtained phase difference. Based on this idea, an AOA measurement system with a phase error of $\pm 2^\circ$ and AOA error of $\pm 0.5^\circ$ is reported [17]. However, since arrayed dual-output modulators, arrayed balanced-photodetectors (BPDs) are required, this approach is relatively complicated, bulky and hard to be integrated on a single chip. [18] reports an AOA measurement method based on optical phase scanning, in which one received microwave signal is directly applied to a phase modulator (PM), and the other received signal is applied to another PM coupled with a low-frequency large-voltage sawtooth-wave signal. Then, the AOA of both single-tone and wideband signal can be estimated by processing the obtained low-frequency electrical signals. In [19], a system that can simultaneously measure both the Doppler frequency shift (DFS) and AOA is proposed, and the error is less than $\pm 1.3^\circ$ for AOA measurement ranging from 0° to 90°.

Manuscript received July 7, 2021; revised September 13, 2021; accepted September 17, 2021. Date of publication September 27, 2021; date of current version December 2, 2021. This work was supported in part by the National Key Research and Development Program of China under Grant 2020YFB1805704, in part by the National Natural Science Foundation of China under Grants 61604072 and 62001218, in part by the National Natural Science Foundation of Jiangsu Province under Grant BK20200436, and in part by the Fundamental Research Funds for the Central Universities. *(Corresponding author: Zhenzhou Tang.)*

Yuanqi Yang, Zhenzhou Tang, Zhongyang Xu, and Shilong Pan are with the Key Laboratory of Radar Imaging and Microwave Photonics, Ministry of Education, Nanjing University of Aeronautics and Astronautics, Nanjing 210016, China (e-mail: yangyuanqi@nuaa.edu.cn; tangzhzh@nuaa.edu.cn; xzy@nuaa.edu.cn; pans@nuaa.edu.cn).

Cui Yu is with the National Key Laboratory of Application Specific Integrated Circuit, Hebei Semiconductor Research Institute, Shijiazhuang 050051, China (e-mail: yucui1@163.com).

Color versions of one or more figures in this article are available at https://doi.org/10.1109/JLT.2021.3115623.

Digital Object Identifier 10.1109/JLT.2021.3115623

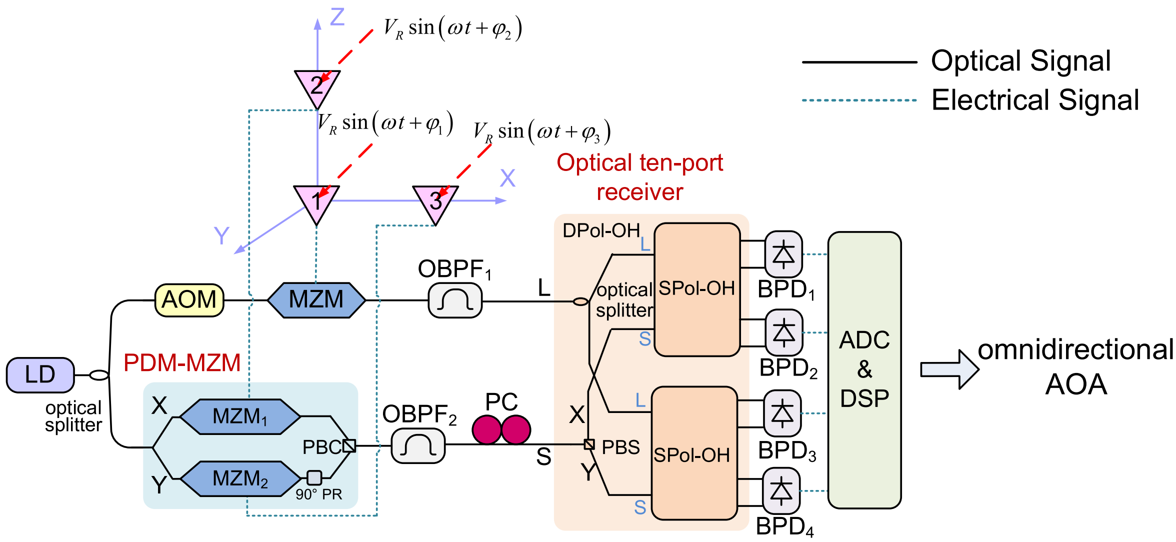

Fig. 1. Schematic diagram of proposed omnidirectional AOA measurement system. LD: laser diode; AOM: acousto-optic modulator; MZM: Mach-Zehnder modulator; PDM-MZM: polarization-division-multiplexed MZM; PBC: polarization beam combiner; OBPF: optical bandpass filter; PC: polarization controller; PBS: polarization beam splitter; SPol-OH: single-polarization 90-degree optical hybrid; DPol-OH: dual-polarization optical hybrid; BPD: balanced photodetector; ADC: analog to digital converter; DSP: digital signal processor; AOA: angle-of-arrival.

In the other category, the AOA information is firstly mapped to other parameters that can be easily measured with cheaper hardware, such as the DC voltage [20]–[22], optical power [23]–[25] and electrical power [26]–[28], to simplify the structure of the system. For example, in [23], [25], the AOA between the two echo signals is mapped to the power of the $\pm1^{st}$-order sidebands at the output of the dual-parallel Mach-Zehnder modulator (DPMZM) [23] or dual-drive MZM (DMZM) [25], by which the maximum measurement error is 1.72° [23] and 2.24° [25], respectively. In [26], two echo signals are sent to two MZMs connected in series and the AOA between the two echo signals is estimated by measuring the power of the output RF signal. The AOA is measured at the range of 0° to over 65° and the measurement error is less than 2.2°. A parallel structure is also reported to measure the AOA [27], which not only removes the incoming microwave signal amplitude dependence, but also has the capability measuring the AOA of multiple microwave signals.

However, in most of the solutions mentioned above, the structures can only use two antennas, which means that the AOA could only be estimated in one dimension. Actually, in order to realize multi-dimensional AOA estimation in a real application system, more antennas are usually needed to build an antenna array [29]. Recently, a 2-D AOA estimation method was reported [30], in which an L-shaped antenna array and a dual-polarization binary phase shift keying modulator are employed. By measuring the optical powers along the orthogonal polarization directions, the AOA in two different dimensions can be respectively obtained with a measurement error of less than ±2.5°. However, omnidirectional AOA estimation is not exactly realized, since its angular range only covers the first octant.

In this paper, an omnidirectional AOA measurement based on an optical ten-port receiver is proposed. In the proposed method, an optical carrier is split into two branches. In one branch, the optical carrier is frequency-shifted by an acoustic-optical modulator (AOM) and then led into an MZM which is modulated by an echo signal from an antenna placed at the original point. In the other branch, a polarization-division-multiplexed MZM (PDM-MZM) is used to imprint the other two echo signals received by the other two antennas located at the *z*-axis, and *x*-axis, respectively. The $+1^{st}$-order sideband in each branch is selected by an optical bandpass filter (OBPF), and then sent to an optical ten-port receiver, which is realized by a dual-polarization optical hybrid (DPol-OH). When four BPDs are connected to the orthogonal outputs of the optical ten-port receiver, two pairs of low-frequency IF signals are obtained. Finally, by processing the obtained IF signals, the azimuth AOA and altitude AOA of the received RF signal could be simultaneously extracted. A proof-of-concept experiment is carried out. Within the altitude angular range of –48.08°∼56.43°, the measurement error of altitude AOA is less than ±1.63°. Besides, the error of azimuth AOA is smaller than ±3.09° when the angular range is ranging from –68.35° to 64.65°.

II. Principle

The schematic of the proposed omnidirectional AOA measurement system is shown in Fig. 1. It mainly includes two parts. One part is an antenna sub-system including three antennas, which is used to receive the RF signals from two different directions. The other part is an optical sub-system based on an optical ten-port receiver, which is employed to realize AOA estimation. The principles and features of each part will be discussed in the following paragraphs.

A. AOA Decomposition Model

Fig. 2 shows the proposed antenna structure located in the coordinate system, consisting of three antennas (T_1, T_2 and T_3) placed at the original point, *z*-axis, and *x*-axis, respectively. The

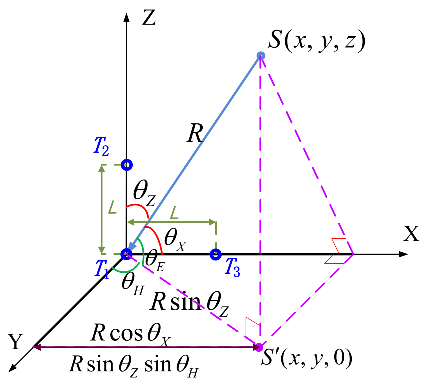

Fig. 2. Proposed antenna structure located in the coordinate system for incoming RF signal vector decomposition when $0°\leq\theta_Z\leq 90°$, $0°\leq\theta_X\leq 90°$.

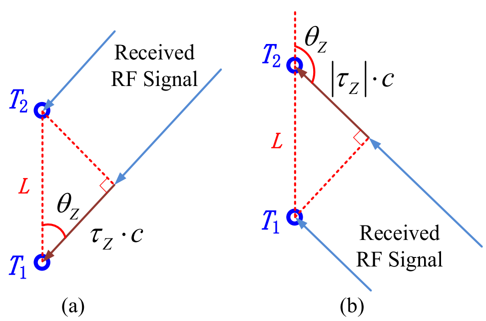

Fig. 3. 1-D AOA measurement by using two antennas when (a) $0\leq\theta_Z\leq 90°$ and (b) $90°\leq\theta_Z\leq 180°$.

distance between the two adjacent antennas is L, that is to say, the positions of the three antennas can be described as $T_1(0, 0, 0)$, $T_2(0, 0, L)$, $T_3(L, 0, 0)$. We assume that the position of the target in this coordinate system is $S(x, y, z)$ and the distance between the target and the original point $O(0, 0, 0)$ is described as R. In most cases, the target is far away from the antennas (i.e., $R>>L$). Thus, the signal paths from the target to the three antennas are approximately parallel to each other, which means that $ST_1//ST_2//ST_3$. As a consequence, 2-D AOA of the target S to each antenna is the same.

In order to calculate the 2-D AOA, the 1-D AOA in plane T_1ST_2 and plane T_1ST_3 should be measured firstly. Fig. 3 shows the 1-D AOA measurement in plane T_1ST_2, in which the two RF signals from the target are received by T_1 and T_2 with a relative time delay τ_Z. As shown in Fig. 3(a), when the AOA θ_Z is less than 90°, the phase shift φ_Z between the two RF signals is caused by this time delay

$$\varphi_Z = \tau_Z \times \omega_{\mathrm{R}} \tag{1}$$

where ω_{R} is the angular frequency of the received RF signal, and the AOA θ_Z can be written as

$$\theta_Z = \cos^{-1}\left(\frac{c\tau_Z}{L}\right) \tag{2}$$

where c is the velocity of electromagnetic radiation in vacuum. In order to avoid the grating lobes in the radiation pattern as well as the phase ambiguity [25], [30], the distance between T_1 and T_2 is usually designed to be $\lambda_{\mathrm{R}}/2$, where λ_{R} is the wavelength of the incoming RF signal. When the space is larger than half of the wavelength, more antennas can be employed to provide different antenna distances in the same dimension for ambiguity elimination [33]. In the proposed system, the absolute value of φ_Z would be no larger than 180°. Thus, (2) can be rewritten as

$$\theta_Z = \cos^{-1}\left(\frac{\varphi_Z}{\pi}\right), \varphi_Z \in [0°, 180°] \tag{3}$$

When $90°\leq\theta_Z\leq 180°$, as shown in Fig. 3(b), the time delay τ_Z is smaller than 0. Thus, the phase shift φ_Z is also less than 0°. In this case θ_Z can be expressed as

$$\theta_Z = \left|\cos^{-1}\left(\frac{c\,|\tau_Z|}{L}\right)\right| = \cos^{-1}\left(\frac{\varphi_Z}{\pi}\right), \varphi_Z \in [-180°, 0°] \tag{4}$$

From (3) and (4), we can summarize that θ_Z can be written as a unified equation

$$\theta_Z = \cos^{-1}\left(\frac{\varphi_Z}{\pi}\right),\ \varphi_Z \in [-180°, 180°] \tag{5}$$

Similarly, the AOA θ_X can also be expressed as

$$\theta_X = \cos^{-1}\left(\frac{\varphi_X}{\pi}\right),\ \varphi_X \in [-180°, 180°] \tag{6}$$

where φ_X is the phase shift between the two RF signals received by T_1 and T_3.

Based on θ_Z, the altitude AOA (θ_E) of the incoming RF signal can be obtained. For instance, when $0°\leq\theta_Z\leq 90°$ (as shown in Fig. 2), θ_E is complementary to θ_Z, so it is given by

$$\theta_E = \sin^{-1}\left(\frac{\varphi_Z}{\pi}\right),\ \varphi_Z \in [0°, 180°] \tag{7}$$

When $90°\leq\theta_Z\leq 180°$, θ_E is supposed to be less than 0°, which has an expression of $\theta_E = 90°–\theta_Z$. In this case, θ_E can be written as

$$\theta_E = -\sin^{-1}\left(\frac{|\varphi_Z|}{\pi}\right) = \sin^{-1}\left(\frac{\varphi_Z}{\pi}\right),\ \varphi_Z \in [-180°, 0°] \tag{8}$$

Apparently, the expression of θ_E would also not change whether the z-coordinate of the target is bigger than 0 or not, i. e.,

$$\theta_E = \sin^{-1}\left(\frac{\varphi_Z}{\pi}\right),\ \varphi_Z \in [-180°, 180°] \tag{9}$$

As for the calculation of the azimuth of the incoming RF signal θ_H, it is dependent to both θ_Z and θ_X according to the geometric relationship. From Fig. 2, when $0°\leq\theta_Z\leq 90°$ and $0°\leq\theta_X\leq 90°$, the x-coordinate of the target S can be written as $x = R\cos\theta_X$, which could also be expressed as $x = R\sin\theta_Z\sin\theta_H$. Thus, θ_H can be expressed as

$$\theta_H = \sin^{-1}\left(\frac{\cos\theta_X}{\sin\theta_Z}\right), \begin{cases} \theta_Z \in [0°, 90°] \\ \theta_X \in [0°, 90°] \end{cases} \tag{10}$$

Then, in the case of $0°\leq\theta_Z\leq 90°$ and $90°\leq\theta_X\leq 180°$, as shown in Fig. 4, θ_H is supposed to be less than 0°. The x-coordinate of the target S can be given by $x = -R\cos(\pi–\theta_X)$ as well as $x =$

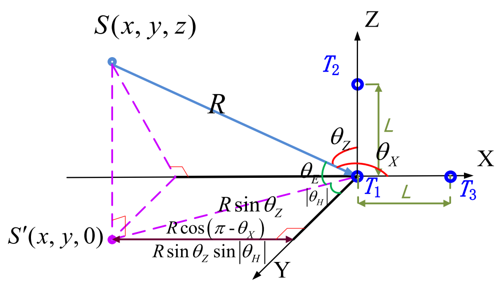

Fig. 4. Proposed antenna structure located in the coordinate system for incoming RF signal vector decomposition when $0°\leq\theta_Z\leq 90°$, $90°\leq\theta_X\leq 180°$.

$-R\sin\theta_Z\sin|\theta_H|$. Therefore, θ_H can be written as

$$\theta_H = \sin^{-1}\left(\frac{\cos\theta_X}{\sin\theta_Z}\right), \begin{cases} \theta_Z \in [0°, 90°] \\ \theta_X \in [90°, 180°] \end{cases} \tag{11}$$

From (10) and (11), the expression of θ_H would not change when $0°\leq\theta_X\leq 180°$. Additionally, no matter the z-coordinate of target S is bigger than 0 or not, $\sin\theta_Z$ always has a non-negative value because of the assumption that $0°\leq\theta_Z\leq 180°$. Hence, in the case of $0°\leq\theta_Z\leq 180°$ and $0°\leq\theta_X\leq 180°$, the expression of θ_H can be summarized as follows

$$\theta_H = \sin^{-1}\left(\frac{\cos\theta_X}{\sin\theta_Z}\right), \begin{cases} \theta_Z \in [0°, 180°] \\ \theta_X \in [0°, 180°] \end{cases} \tag{12}$$

After substituting the expression of θ_Z and θ_X, (12) could be rewritten as

$$\theta_H = \sin^{-1}\left(\frac{\varphi_X}{\sqrt{\pi^2 - \varphi_Z{}^2}}\right), \begin{cases} \varphi_Z \in [-180°, 180°] \\ \varphi_X \in [-180°, 180°] \end{cases} \tag{13}$$

To sum up, from (9), and (13), by monitoring the phase shift φ_Z and φ_X, azimuth AOA (θ_H) and altitude AOA (θ_E) of the received RF signal can be calculated. Since both angular ranges cover two quadrants, 2-D AOA estimation can be realized in four octants, meaning that omnidirectional AOA estimation could be successfully achieved.

B. Principle of Omnidirectional AOA Measurement

In the optical sub-system, an optical carrier with an angular frequency of ω_c and an amplitude of E_c is emitted by a laser diode (LD) and is split into two branches by a 1:1 optical splitter. In the upper branch, the optical carrier is frequency-shifted by an AOM, thus the optical carrier can be written as

$$E_c(t) = \frac{E_c}{\sqrt{2}}\exp\left(j\omega_c t + j\omega_S t\right) \tag{14}$$

where ω_S represents the angular frequency introduced by the AOM. Then the frequency-shifted optical carrier is fed into an MZM, which is driven by the RF signal received by T_1. In order to suppress the optical carrier, the MZM is biased at the minimum transmission point, so the modulated optical signal is given by

$$E_1(t) = \frac{E_c}{\sqrt{2}}\begin{bmatrix} J_1(m_R)\exp\left(j\omega_c t + j\omega_S t + j\omega_R t + j\varphi_1\right) \\ +J_{-1}(m_R)\exp\left(j\omega_c t + j\omega_S t - j\omega_R t - j\varphi_1\right) \end{bmatrix} \tag{15}$$

where ω_R and φ_1 are the angular frequency and phase of the received RF signal. $J_n(\cdot)$ is the first kind of Bessel function and $m_R = \pi V_R/V_\pi$ is the modulation index, where V_R is the amplitude of the incoming RF signal and V_π denotes the half-wave voltage of the MZM.

Then an OBPF (OBPF_1) is connected after the MZM to select the $+1^{\text{st}}$-order sideband, which can be written as

$$E_{1f}(t) = \frac{E_c}{\sqrt{2}}\left[J_1(m_R)\exp\left(j\omega_c t + j\omega_S t + j\omega_R t + j\varphi_1\right)\right] \tag{16}$$

In the lower branch, the optical carrier is fed into a PDM-MZM, which integrates two MZMs along the two orthogonal polarization directions. Then, the incoming RF signal with an amplitude of V_R received by T_2 and T_3 are sent to the RF input ports of each MZM respectively, which can be expressed as

$$\begin{bmatrix} V_2(t) \\ V_3(t) \end{bmatrix} = V_R\begin{bmatrix} \sin\left(\omega_R t + \varphi_2\right) \\ \sin\left(\omega_R t + \varphi_3\right) \end{bmatrix} \tag{17}$$

where φ_2 and φ_3 are the phases of the incoming RF signal arrived at T_2 and T_3. When the MZMs are also biased at the minimum transmission point, the modulated signal at the output of the PDM-MZM can be given by

$$\begin{Bmatrix} E_x(t) \\ E_y(t) \end{Bmatrix} = \frac{E_c}{2}\left\{\begin{matrix} \begin{bmatrix} J_1(m_R)\exp\left(j\omega_c t + j\omega_R t + j\varphi_2\right) \\ +J_{-1}(m_R)\exp\left(j\omega_c t - j\omega_R t - j\varphi_2\right) \end{bmatrix}\vec{e}_x \\ \begin{bmatrix} J_1(m_R)\exp\left(j\omega_c t + j\omega_R t + j\varphi_3\right) \\ +J_{-1}(m_R)\exp\left(j\omega_c t - j\omega_R t - j\varphi_3\right) \end{bmatrix}\vec{e}_y \end{matrix}\right\} \tag{18}$$

where $\vec{e}_x$ and $\vec{e}_y$ are two orthogonal basic vectors, which represent two orthogonal polarization states, respectively.

Similar to the upper branch, the recombined modulated optical signal is sent to another OBPF (OBPF_2) to select the $+1^{\text{st}}$-order sidebands, which is yielded as

$$\begin{Bmatrix} E_{xf}(t) \\ E_{yf}(t) \end{Bmatrix} = \frac{E_c}{2}\begin{Bmatrix} \left[J_1(m_R)\exp\left(j\omega_c t + j\omega_R t + j\varphi_2\right)\right]\vec{e}_x \\ \left[J_1(m_R)\exp\left(j\omega_c t + j\omega_R t + j\varphi_3\right)\right]\vec{e}_y \end{Bmatrix} \tag{19}$$

Then, the output signals of OBPF_1 and OBPF_2 are sent to the L-port and the S-port of the DPol-OH, respectively. As can be seen from Fig. 1, inside of the DPol-OH, a polarization beam splitter (PBS) is integrated at the S-port. Thus, by using a polarization controller (PC) to properly adjust the polarization state, the polarization-division-multiplexed signal sent to the S-port can be separated into two orthogonal parts. Then, the two orthogonal signals are sent to the S-port of each single-polarization 90-degree optical hybrid (SPol-OH) inside the DPol-OH. Besides, an optical splitter is integrated at the L-port, so the optical signal sent to the L-port is directly split into two portions, and sent to the L-port of each SPol-OH.

In order to realize coherent detections, two BPDs are connected at the output ports of each SPol-OH. In particular, the output signals of BPD_1 and BPD_2 is a pair of quadrature signals of the *X*-polarization direction, which can be expressed as

$$\begin{Bmatrix} I_X \\ Q_X \end{Bmatrix} \propto \begin{Bmatrix} \cos(\omega_S t + \varphi_2 - \varphi_1) \\ \sin(\omega_S t + \varphi_2 - \varphi_1) \end{Bmatrix} \tag{20}$$

As mentioned above, φ_Z represents the phase shift between the two incoming RF signals arrived at T_1 and T_2, which can also be expressed as $\varphi_Z = \varphi_2 – \varphi_1$. Hence, (20) can be rewritten as

$$\begin{Bmatrix} I_X \\ Q_X \end{Bmatrix} \propto \begin{Bmatrix} \cos(\omega_S t + \varphi_Z) \\ \sin(\omega_S t + \varphi_Z) \end{Bmatrix} \tag{21}$$

Since ω_S is the known angular frequency introduced by the AOM, the value of φ_Z can be easily calculated by performing $\tan^{-1}(Q_X/I_X)$.

Similarly, since the phase shift φ_X between the two incoming RF signals arrived at T_1 and T_3 equals to φ_3–φ_1, the quadrature signals obtained by BPD_3 and BPD_4 along the *Y*-polarization direction can be given by

$$\begin{Bmatrix} I_Y \\ Q_Y \end{Bmatrix} \propto \begin{Bmatrix} \cos(\omega_S t + \varphi_3 - \varphi_1) \\ \sin(\omega_S t + \varphi_3 - \varphi_1) \end{Bmatrix} = \begin{Bmatrix} \cos(\omega_S t + \varphi_X) \\ \sin(\omega_S t + \varphi_X) \end{Bmatrix} \tag{22}$$

Likewise, φ_X can be readily got by performing $\tan^{-1}(Q_Y/I_Y)$. Therefore, based on φ_Z and φ_X, the azimuth AOA (θ_H) and altitude AOA (θ_E) of the incoming RF signal can be calculated according to (9) and (13).

III. Experimental Results

A proof-of-concept experiment is carried out based on Fig. 1. A continuous wave light source is generated by an LD (TeraXion Inc.) and split into two branches by a 50:50 optical coupler. The wavelength and power of the light source is 1550.128 nm and 16 dBm. In the upper branch, an AOM is employed to introduce an 80-MHz auxiliary frequency shift by a microwave source (Aglient E4421B). The output signal of the AOM is then transmitted to an MZM (Fujitsu FTM7938) with a bandwidth of >25 GHz and a half-wave voltage of <2.8 V. Then the output signal of the MZM is transmitted to an OBPF (OBPF_1, Yenista XTM-50) to select the $+1^{\mathrm{st}}$-order sideband after being amplified by an erbium-doped optical fiber amplifier (EDFA_1). The output of OBPF_1 is then sent to the *L*-port of a DPol-OH (Kylia COH28). In the lower branch, the optical carrier is sent to a PDM-MZM (Fujitsu FTM7977) with a bandwidth of >23 GHz and a half-wave voltage of <3.5 V. Another OBPF (OBPF_2, Yenista XTM-50) is used to select $+1^{\mathrm{st}}$-order sidebands of the output signal of the PDM-MZM after being amplified by another EDFA (EDFA_2). Then the selected sidebands are sent to *S*-port of the DPol-OH.

To emulate the incoming RF signals of different phases received by the three antennas, a 20 GHz microwave signal with a power of 25 dBm is generated by another microwave source (Keysight N5183B) and is split into three parts. One part is sent to the RF input port of the MZM to emulate the incoming RF signal received by T_1, while the other two parts are sent to the two sub-MZMs of the PDM-MZM to emulate the incoming RF signals received by T_2 and T_3, respectively. It should be noted that a voltage-controlled microwave phase shifter is inserted in

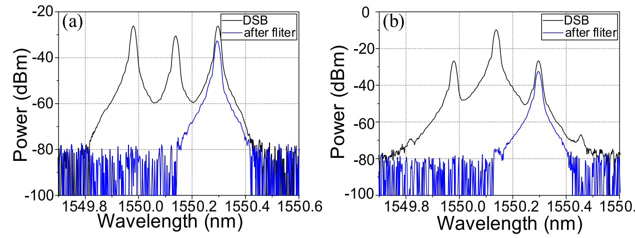

Fig. 5. Optical spectra measured from the (a) lower and (b) upper branch.

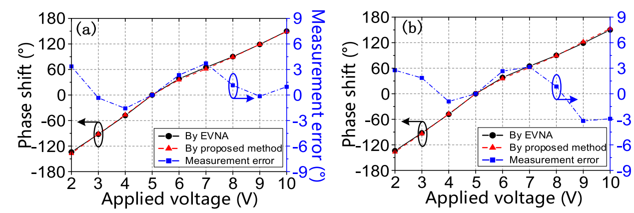

Fig. 6. Phase shifts (a) φ_Z and (b) φ_X measured by EVNA (solid line) and the proposed method (dashed line) and the corresponding measurement error (dash-dotted line).

each branch to introduce a variable AOA between the received RF signals. Four low-speed BPDs (Thorlab PDB450) are connected to the output ports of the DPol-OH to realize coherent I/Q detections. Then the output signals of the four BPDs are sent to a real-time oscilloscope (Keysight DSO-X92504A) to perform analog-to-digital converter (ADC) and digital signal processing. An optical spectrum analyzer (YOKOGAWA AQ6370) is employed to observe the optical spectrum. It is worth noting that, although a high-speed oscilloscope is used in the experiment, it is not necessary because the auxiliary frequency is relatively low, so the digital procession can be easy and cheap.

The optical spectrum measured from the upper branch is shown in Fig. 5(a). As can be seen, the optical carrier and the unwanted sidebands is largely suppressed by biasing the MZM at the minimum transmission point and adjusting the central wavelength of OBPF_1 to align around the wavelength of the $+1^{\mathrm{st}}$-order sideband. Similarly, in the lower branch, the $+1^{\mathrm{st}}$-order sideband of the polarization-division-multiplexed signal is selected by OBPF_2, which is shown in Fig. 5(b). Again, the optical carrier is also suppressed in this branch, so the interference between the two branches when they are combined in the DPol-OH can be avoided.

According to Section II, φ_Z and φ_X can be independently obtained by measuring the phase of the IF signals obtained from the *X*- and *Y*- polarization outputs. So, firstly, we only adjust the phase shifter connected to MZM_1 to introduce a phase difference between the RF signals applied to MZM and MZM_1. By analyzing the output signals of BPD_1 and BPD_2 according to Section II, the phase shift φ_Z is monitored. In order to verify the accuracy of our system, we also measured the phase shift versus the applied DC voltage to the phase shifter by an electrical vector network analyzer (EVNA, R&S ZVA-67), which is shown as the solid line (symbol •) in Fig. 6(a). The phase shift φ_Z measured by our proposed system is demonstrated as the dashed line (symbol ▲) in Fig. 6(a), and the corresponding measurement error is also

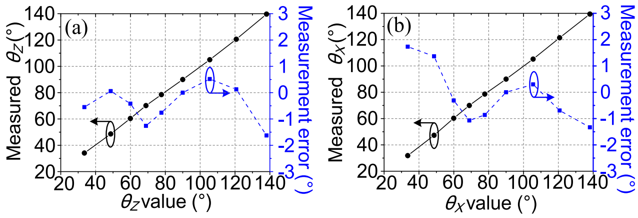

Fig. 7. AOA (a) θ_Z and (b) θ_X calculated from measured phase shifts φ_Z and φ_X (solid line) the corresponding measurement error (dashed line).

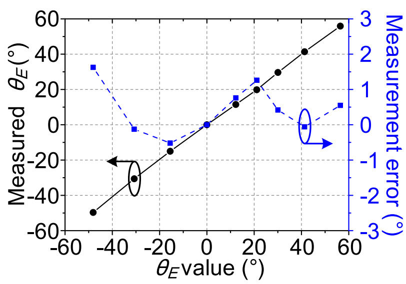

Fig. 8. Measured θ_E and the measurement error.

depicted as the dash-dotted line (symbol ■). The measurement error of φ_Z is less than $\pm 3.71°$, within the angular range of $-133.94° \sim 149.98°$.

Secondly, the phase shifter connected to MZM_2 is adjusted to introduce a phase difference between the RF signals applied to MZM and MZM_2. In this condition, the phase shift φ_X is measured by computing the output signals of BPD_3 and BPD_4 according to Section II. Similar to Fig. 6(a), by comparing with the phase shift measured by an electrical vector network analyzer (solid line, symbol •), the corresponding measurement error is show as the dash-dotted line (symbol ■) in Fig. 6(b), which is $\pm 3.19°$ within the angular range of $-133.94° \sim 149.98°$.

Based on the measured values of φ_Z and φ_X, the measured value and measurement error of θ_Z and θ_X could be got by substituting them into the equation (5) and (6). As is shown in Fig. 7, the measurement error of AOA θ_Z within the angular range of $33.57° \sim 138.08°$ is less than $\pm 1.63°$, while the measurement error of AOA θ_X is smaller than $\pm 1.73°$ within the same angular range.

Since we already get θ_Z, the altitude AOA (θ_E) can be easily got according to (7), since θ_E is complementary to θ_Z. The measured θ_E and measurement error are shown in Fig. 8, which is less than $\pm 1.63°$ within the angular range of $-48.08° \sim 56.43°$.

The calculation of θ_{H} is much more complex, because θ_{H} is a numerical result coming from the value of θ_Z and θ_X. Moreover, according to (12), only if $|\cos\theta_X| \leq |\sin\theta_Z|$ can θ_{H} be calculated, which means that θ_Z and θ_X have to satisfy the following conditions.

$$\begin{cases} 90° \leq \theta_X + \theta_Z \leq 270° \\ 90° \leq |\theta_X - \theta_Z| \leq 270° \end{cases} \tag{23}$$

The result of the calculated θ_{H} is shown in Fig. 9(a). The measurement error of θ_{H} is also calculated according the measurement result and error of θ_Z and θ_X, which is shown in

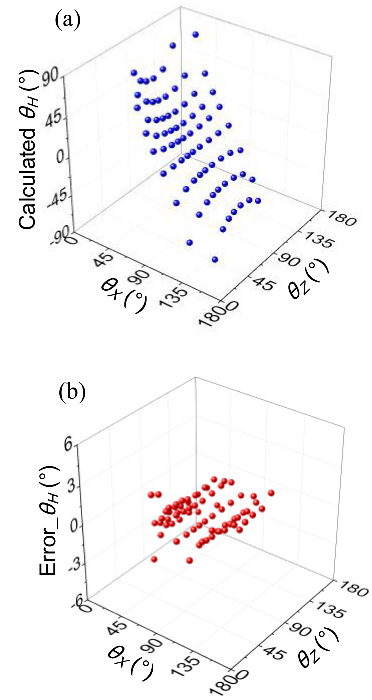

Fig. 9. (a) Calculated θ_H and (b) the measurement error.

Fig. 9(b). Within the angular range of $-68.35° \sim 64.65°$, the measurement error of θ_H is less than $\pm 3.09°$, which is worse than the measurement error of either θ_Z or θ_X. This is due to the error propagation law when calculating the value of θ_H [31], which will be discussed in the next section.

IV. Discussion

A. Comparison With the State-of-the-art

Table I shows the comparison with the state-of-the-art. As a microwave photonic system, the proposed method has the advantages of being able to achieve high frequency, large bandwidth and anti-electromagnetic interference, compared to the electrical AOA measurement methods. In comparison to the previous photonics-based system, an omnidirectional 2-D AOA measurement covering the four octants is firstly realized.

B. Error Propagation

As is mentioned in Section III, unlike θ_E, the measurement of is θ_H calculated from θ_Z and θ_X according to (12). When the measurement error is taken into consideration, the measurement results of θ_Z and θ_X could be written as

$$\begin{bmatrix} \theta_{Zm} \\ \theta_{Xm} \end{bmatrix} = \begin{bmatrix} \theta_Z \pm \Delta\theta_Z \\ \theta_X \pm \Delta\theta_X \end{bmatrix} \tag{24}$$

where θ_Z and θ_X are the accurate value, while $\Delta\theta_Z$ and $\Delta\theta_X$ represent the measurement error. As is known to all, when calculating θ_{Hm} from the measured values of θ_{Zm} and θ_{Xm}, an inevitable error propagation would occur [31] thus the calculated result of the azimuth AOA can also be expressed as

$$\theta_{Hm} = \theta_H \pm \Delta\theta_H \tag{25}$$

TABLE I
THE COMPARISON WITH OTHER STATE-OF-ART AOA MEASUREMENT TECHNIQUES

Domain	Technology	Theoretical measurement range	AOA Range	Maximum measurement error	DIM
Electrical	6-port [9]	-90°~90°	-90°~90°	0.518°	1-D
Electrical	8-port [10]	-90°~90°(altitude) -90°~90°(azimuth)	-5°~5° (altitude) -5°~5° (azimuth)	0.4°	2-D
Optical	DMZM+OTF [18]	0°~90°	0°~90°	4.45°	1-D
Optical	PDM-MZM+OBPF [19]	0°~90°	0°~90°	1.3°	1-D
Optical	PDM-MZM [20]	0°~90°	0°~65°	2.5°	1-D
Optical	DPMZM+ONF [22]	0°~180°	0°~160°	3.5°	1-D
Optical	DPMZM+WDM [25]	0°~180°	0°~165°	2.24°	1-D
Optical	MZM+DMZM+OF [26]	0°~90°	0°~65°	1.9°	1-D
Optical	DP-BPSKM [30]	0°~90°(altitude) 0°~90°(azimuth)	0°~71.78°(1-D) 0°~71.78°(2-D)	1° (1-D) 2.2° (2-D)	2-D
Optical	MZM+OBPF+PDM-MZM [This work]	-90°~90°(altitude) -90°~90°(azimuth)	-48.08°~56.43° (altitude) -68.35° to 64.65°(azimuth)	1.63° (1-D) 3.09° (2-D)	2-D

DIM: dimension; MZM: Mach-Zehnder modulator; DMZM: dual-driven MZM; PDM-MZM: polarization-division-multiplexed MZM; DPMZM: dual-parallel Mach-Zehnder modulator; OTF: optical tunable filter; ONF: optical notch filter; WDM: wavelength division multiplexer; OF: optical filter; DP-BPSKM: dual polarization binary phase shift keying modulator.

where θ_H and $\Delta\theta_H$ represent the accurate result and the error of the azimuth AOA, respectively. Hence according to the law of error propagation, $\Delta\theta_H$ can be expressed as

$$\Delta\theta_H = \pm\sqrt{\left(\frac{\partial\theta_H}{\partial\theta_X}\right)^2(\Delta\theta_X)^2+\left(\frac{\partial\theta_H}{\partial\theta_Z}\right)^2(\Delta\theta_Z)^2}$$
$$= \pm\sqrt{\frac{\sin^2\theta_X\sin^2\theta_Z(\Delta\theta_X)^2+\cos^2\theta_X\cos^2\theta_Z(\Delta\theta_Z)^2}{\sin^4\theta_Z-\sin^2\theta_Z\cos^2\theta_X}} \tag{26}$$

Since the error of azimuth AOA θ_H is determined by the measurement error of θ_Z and θ_X, it is reasonable for $\Delta\theta_H$ to be larger than either of θ_Z or θ_X. In our experimental results, the measurement error of θ_H is within ±3.09° while the error of either θ_Z or θ_X is less than ±1.73°, which agrees with the law of error propagation.

C. Effect of Polarization Crosstalk

As can be seen from our experimental results, the measurement error is still relatively high, compared to the published 1-D AOA estimation methods [20]–[28]. This error can be considered to be mainly caused by polarization crosstalk. In our experiment, we adjust the PC to separate the polarization-division-multiplexed signal into two orthogonal parts. However, in practical experiments, it is difficult to achieve the complete separation of the two polarization states, which means that the polarization crosstalk is inevitable.

Since polarization dependent loss (PDL) and polarization mode dispersion (PMD) are only significant in long-haul transmission system [32], we neglect them in our analysis for the moment. In our present scenario, the changes of the polarization state could be described as a rotation matrix **R** according to

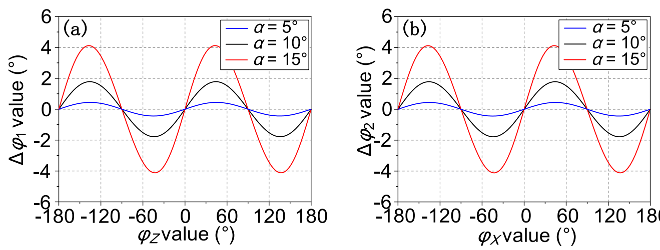

Fig. 10. The simulated phase difference between (a) I_X and I'_X when $\varphi_X = 0°$ and (b) I_Y and I'_Y when $\varphi_Z = 0°$.

$$\begin{bmatrix}E'_{xf}(t)\\E'_{yf}(t)\end{bmatrix} = \mathbf{R}\begin{bmatrix}E_{xf}(t)\\E_{yf}(t)\end{bmatrix} = \begin{bmatrix}\cos\alpha & -\sin\alpha\\ \sin\alpha & \cos\alpha\end{bmatrix}\begin{bmatrix}E_{xf}(t)\\E_{yf}(t)\end{bmatrix} \tag{27}$$

where E'_{xf} and E'_{yf} represent the separated two parts of the polarization-division-multiplexed signal after the PBS inside the DPol-OH, and α is the error rotation angle ($0 \le \alpha < \pi/2$). Based on (19), E'_{xf} and E'_{yf} can be written as

$$\begin{Bmatrix}E'_{xf}(t)\\E'_{yf}(t)\end{Bmatrix} \propto \begin{Bmatrix}\exp(j\omega_R t + j\varphi_2)\cos\alpha - \exp(j\omega_R t + j\varphi_3)\sin\alpha\\ \exp(j\omega_R t + j\varphi_3)\cos\alpha + \exp(j\omega_R t + j\varphi_2)\sin\alpha\end{Bmatrix} \tag{28}$$

Then, the output of BPD_1 and BPD_3 can be described as

$$\begin{Bmatrix}I'_X\\I'_Y\end{Bmatrix} \propto \begin{Bmatrix}\cos(\omega_S t + \varphi_Z)\cos\alpha - \cos(\omega_S t + \varphi_X)\sin\alpha\\ \cos(\omega_S t + \varphi_X)\cos\alpha + \cos(\omega_S t + \varphi_Z)\sin\alpha\end{Bmatrix} \tag{29}$$

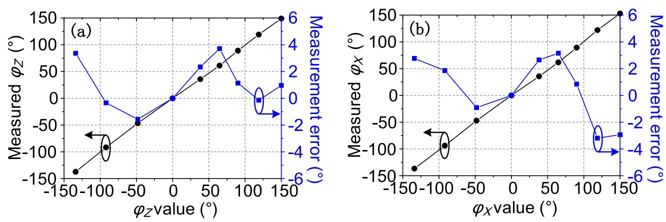

Fig. 11. Phase shifts (a) φ_Z and (b) φ_X measured by the proposed method and the corresponding measurement error.

Fig. 10(a) shows the phase error $\Delta\varphi_1$ between I_X and I'_X, when the phase φ_Z changes from 0° to 180° and the phase φ_X is fixed at 0°. As can be seen from Fig. 10(a), when α is set to 5°, 10° and 15°, the maximum value of the phase error $\Delta\varphi_1$ between I_X and I'_X is 0.44°, 1.78° and 4.11°. The value of $\Delta\varphi_1$ has a *Sine*-liked shape, with a period of 180°. We also simulate the situation when φ_Z is fixed at 0° and φ_X changes from 0° to 180°. The phase error $\Delta\varphi_2$ between I_Y and I'_Y is shown in Fig. 10(b), which is nearly the same as $\Delta\varphi_1$ in Fig. 10(a).

In our experimental results, the measurement errors of φ_Z and φ_X also has a nearly *Sin*-liked fluctuation, as shown in Fig. 11, which agrees with our simulation. Hence, the polarization crosstalk does have a significant effect on the experimental results, which should be avoided more carefully in further research, for example using optical devices with lower polarization crosstalk.

Currently, the system is based on the discrete components, which makes the system complicated and bulky. Therefore, a straightforward way to reduce the SWaP of the system is to use photonic integration. All the main devices, such as the modulators, optical filters, optical hybrids and photodetectors, can be integrated in a single platform, for example, the SOI platform. Furthermore, it should be noted that, if the devices can be integrated on a single chip, separate MZMs and optical hybrids, instead of the PDM-MZM and DPol-OH in the discrete fiber system, can be considered to solve the polarization crosstalk problem as well.

V. Conclusion

In summary, we have proposed and experimentally demonstrated a photonic method to measure omnidirectional AOA based on optical ten-port receiver. The altitude and azimuth AOA can be simultaneously obtained in four octants. In the proof-of-concept experiment, within the angular range of $-48.08°\sim56.43°$, the error of the altitude AOA is less than $\pm1.63°$, while the error of the azimuth AOA is smaller than $\pm3.09°$ when the angular range changes from $-68.35°$ to $64.65°$.

References

[1] Y. Li, J. Liu, B. Cao, and C. Wang, "Joint optimization of radio and virtual machine resources with uncertain user demands in mobile cloud computing," *IEEE Trans. Multimedia*, vol. 20, no. 9, pp. 2427–2438, Sep. 2018.

[2] W. Saad, M. Bennis, and M. Chen, "A vision of 6G wireless systems: Applications trends technologies and open research problems," *IEEE Netw.,* vol. 34, no. 3, pp. 134–142, May 2020.

[3] S. Li, L. Xu, and S. Zhao, "5G Internet of Things: A survey," *J. Ind. Inf. Integr.*, vol. 10, pp. 1–9, Jun. 2018.

[4] W. Xia, Y. Li, and S. Dong, "Radar-based high-accuracy cardiac activity sensing," *IEEE Trans. Instrum. Meas.,* vol. 70, pp. 1–13, Jan. 2021.

[5] Z. Tang and S. Pan, "Simultaneous measurement of Doppler-frequency-shift and angle-of-arrival of microwave signals for automotive radars," in *Proc. Int. Topical Meeting Microw. Photon.*, 2019, pp. 1–4.

[6] G. Krishnan, R. Joshi, T. O'Connor, F. Pla, and B. Javidi, "Human gesture recognition under degraded environments using 3D-integral imaging and deep learning," *Opt. Exp.,* vol. 28, no. 13, pp. 19711–19725, Jun. 2020.

[7] J. Saluja, J. Casanova, and J. Lin, "A supervised machine learning algorithm for heart-rate detection using Doppler motion-sensing radar," *IEEE J. Electromagn. RF Microw. Med. Biol.*, vol. 4, no. 1, pp. 45–51, Mar. 2020.

[8] D. J. McFarland and J. R. Wolpaw, "EEG-based brain–computer interfaces," *Curr. Opin. Biomed. Eng.*, vol. 4, pp. 194–200, Dec. 2017.

[9] J. Moghaddasi, T. Djerafi, and K. Wu, "Multiport interferometer-enabled 2-D angle of arrival (AOA) estimation system," *IEEE Trans. Microw. Theory Techn.*, vol. 65, no. 5, pp. 1767–1779, May 2017.

[10] B. Habib, M. Mohsin, and M. S. Arif, "A novel approach for UWB passive direction finding using 6 port network," in *Proc. 2nd Int. Conf. Latest Trends Elect. Eng. Comput. Technol*., 2019, pp. 1–6.

[11] J. Yao, "Microwave photonics," *J. Lightw. Technol.*, vol. 27, no. 3, pp. 314–335, Feb. 2009.

[12] J. Capmany and D. Novak, "Microwave photonics combines two worlds," *Nat. Photon,* vol. 1, pp. 319–330, Jun. 2007.

[13] Y. Men, A. Wen, Y. Li, and Y. Tong, "Photonic approach to flexible multi-band linearly frequency modulated microwave signals generation," *Opt. Lett.*, vol. 46, no. 7, pp. 1696–1699, Apr. 2021.

[14] T. Lin *et al.*, "Microwave photonics time-delayed mixer," *J. Lightw. Technol.*, vol. 39, no. 10, pp. 3145–3153, May 2021.

[15] S. Pan and Y. Zhang, "Microwave photonic radars," *J. Lightw. Technol.*, vol. 38, no. 19, pp. 5450–5484, Oct. 2020.

[16] S. Pan, X. Ye, Y. Zhang, and F. Zhang, "Microwave photonic array radars," *IEEE J. Microw.,* vol. 1, no. 1, pp. 176–190, Jan. 2021.

[17] P. D. Biernacki, A. Ward, L. T. Nichols, and R. D. Esman, "Microwave phase detection for angle of arrival detection using a 4-channel optical downconverter," in *Proc. Int. Topical Meeting Microw. Photon.*, 1998, pp. 137–140.

[18] P. Li *et al.*, "Angle-of-arrival estimation of microwave signals based on optical phase scanning," *J. Lightw. Technol.*, vol. 37, no. 24, pp. 6048–6053, Dec. 2019.

[19] J. Zhao, Z. Tang, and S. Pan, "Photonic approach for simultaneous measurement of microwave DFS and AOA," *Appl. Opt.*, vol. 60, no. 16, pp. 4622–4626, May 2021.

[20] H. Chen and E. H. Chan, "Photonics-based CW/pulsed microwave signal AOA measurement system," *J. Lightw. Technol.*, vol. 38, no. 8, pp. 2292–2298, Apr. 2020.

[21] P. Li *et al.*, "Photonic approach for simultaneous measurements of Doppler-frequency-shift and angle-of-arrival of microwave signals," *Opt. Exp.,* vol. 27, no. 6, pp. 8709–8716, Mar. 2019.

[22] H. Chen and E. H. Chan, "Simple approach to measure angle of arrival of a microwave signal," *IEEE Photon. Technol. Lett.*, vol. 31, no. 22, pp. 1795–1798, Nov. 2019.

[23] Q. Ma, X. Zhao, Z. Cao, Y. Liu, and Y. Xiang, "Accuracy monitoring and enhancement for microwave localization using parallel optical delay detector," *Opt. Commun.*, vol. 439, pp. 94–98, May 2019.

[24] Z. Cao *et al.*, "Phase modulation parallel optical delay detector for microwave angle-of-arrival measurement with accuracy monitored," *Opt. Lett.,* vol. 39, no. 6, pp. 1497–1500, Mar. 2014.

[25] H. Zhuo, A. Wen, and Y. Wang, "Photonic angle-of-arrival measurement without direction ambiguity based on a dual-parallel Mach–Zehnder modulator," *Opt. Commun.,* vol. 451, pp. 286–289, Nov. 2019.

[26] H. Chen and E. H. W. Chan, "Angle-of-arrival measurement system using double RF modulation technique," *IEEE Photon. J.*, vol. 11, no. 1, pp. 1–10, Feb. 2019.

[27] H. Chen, C. Huang, and E. H. W. Chan, "Photonic approach for measuring AOA of multiple signals with improved measurement accuracy," *IEEE Photon. J.*, vol. 12, no. 3, pp. 1–10, Jun. 2020.

[28] H. Zhuo and A. Wen, "A photonic approach for Doppler-frequency-shift and angle-of-arrival measurement without direction ambiguity," *J. Lightw. Technol.*, vol. 39, no. 6, pp. 1688–1695, Mar. 2021.

[29] R. Amiri, F. Behnia, and H. Zamani, "Efficient 3-D positioning using time-delay and AOA measurements in MIMO radar systems," *IEEE Commun. Lett.,* vol. 21, no. 12, pp. 2614–2617, Dec. 2017.

[30] T. Lin *et al.*, "Photonic 2-D angle-of-arrival estimation based on an L-shaped antenna array for an early radar warning receiver," *Opt. Exp.,* vol. 28, no. 26, pp. 38960–38972, Dec. 2020.
[31] J. M. McCormick, "Propagation of error," Aug. 2010. [Online]. Available: https://chemlab.truman.edu/data-analysis/propagation-of-error/
[32] R. Schmogrow, P. C. Schindler, C. Koos, W. Freude, and J. Leuthold, "Blind polarization demultiplexing with low computational complexity," *IEEE Photon. Technol. Lett.,* vol. 25, no. 13, pp. 1230–1233, Jul. 2013.
[33] A. Koelpin *et al.*, "Six-port based interferometry for precise radar and sensing applications," *Sensors*, vol. 16, no. 10, pp. 1556, Sep. 2016.

Yuanqi Yang received the B.S. degree in 2019 in information engineering from the Nanjing University of Aeronautics and Astronautics, Nanjing, China, where he is currently working toward the third-year Postgraduate degree with the Key Laboratory of Radar Imaging and Microwave Photonics, Ministry of Education. His research focuses on photonic multiport receivers and their applications in non-contact sensing.

Zhenzhou Tang (Member, IEEE) received the M.S. degree in information engineering from the Nanjing University of Aeronautics and Astronautics, Nanjing, China, in 2014 and the double Ph.D. degrees in communication and information system from the Nanjing University of Aeronautics and Astronautics and in photonics engineering from Ghent University, Belgium, in 2019 and 2020, respectively. He is currently an Associate Professor with the Key Laboratory of Radar Imaging and Microwave Photonics, Ministry of Education, Nanjing University of Aeronautics and Astronautics. He has authored or coauthored more than 30 research papers, including more than 15 papers in peer-reviewed journals and 15 papers in conference proceedings. His research interests include photonics-based microwave mixing, photonic integrated circuits, and radio over fiber communications. He is one of the recipients of the 2017 IEEE Photonics Society Graduate Student Fellowship.

Zhongyang Xu (Member, IEEE) received the B.S. degree in physics from Sun Yat-sen University, Guangzhou, China, and the Ph.D. degree in physics from Tsinghua University, Beijing, China, in 2010 and 2015, respectively. He is currently a Lecturer with the College of Electronic and Information Engineering, Nanjing University of Aeronautics and Astronautics, Nanjing, China. His current research interests include frequency-modulated continuous-wave (FMCW) detection and radio over free-space optics (RoFSO).

Cui Yu received the Ph.D. degree in material science from Zhejiang University, Hangzhou, China, in 2011. She is a Doctor and Professor. In the same year, she joined the National Key Laboratory of ASIC, Hebei Semiconductor Research Institute, China. She has authored and coauthored more than 50 papers in SCI/EI-indexed journals. Her research interests include graphene and diamond materials and their field-effect transistor devices and application.

Shilong Pan (Senior Member, IEEE) received the B.S. and Ph.D. degrees in electronic engineering from Tsinghua University, Beijing, China, in 2004 and 2008, respectively. From 2008 to 2010, he was a Vision 2010 Postdoctoral Research Fellow with the Microwave Photonics Research Laboratory, University of Ottawa, Ottawa, ON, Canada. In 2010, he joined the College of Electronic and Information Engineering, Nanjing University of Aeronautics and Astronautics, Nanjing, China, where he is currently a Full Professor and an Executive Director of the Key Laboratory of Radar Imaging and Microwave Photonics, Ministry of Education.

He has authored or coauthored more than 280 papers in peer-reviewed journals and 200 papers in conference proceedings. His research interests include microwave photonics which includes optical generation and processing of microwave signals, analog photonic links, photonic microwave measurement, and integrated microwave photonics.

Prof. Pan is currently an Associate Editor for the Electronics Letters, a Topical Editor of the Chinese Optics Letters and PhotoniX, and is the Vice Chair of the IEEE MTT-22 Microwave Photonics. He is a Member of the IEEE MTT-S publication committee and a Steering Committe Member of the IEEE/OSA JOURNAL OF LIGHTWAVE TECHNOLOGY. Prof. Pan was the Chair of a number of international conferences, symposia, and workshops, including the TPC Chair of the International Conference on Optical Communications and Networks in 2015, TPC Co-Chair of the IEEE International Topical Meeting on Microwave Photonics (MWP) in 2017, and the General Co-Chair of IEEE MWP 2021.

Prof. Pan is a Fellow of OSA, SPIE, and IET. He was selected as an IEEE Photonics Society Distinguished Lecturer in 2019 and was the recipient of the IEEE MTT-S Outstanding Young Engineer Award in 2021.